

2022-02-05

# Detection of a Double-Stranded MGMT Gene Using Electrochemically Reduced Graphene Oxide (ErGO) Electrodes Decorated with AuNPs and Peptide Nucleic Acids (PNA)

Safarzadeh, Mina

<http://hdl.handle.net/10026.1/18720>

---

10.3390/bios12020098

Biosensors

MDPI AG

---

*All content in PEARL is protected by copyright law. Author manuscripts are made available in accordance with publisher policies. Please cite only the published version using the details provided on the item record or document. In the absence of an open licence (e.g. Creative Commons), permissions for further reuse of content should be sought from the publisher or author.*

## Article

# Detection of a Double-Stranded MGMT Gene Using Electrochemically Reduced Graphene Oxide (ErGO) Electrodes Decorated with AuNPs and Peptide Nucleic Acids (PNA)

Mina Safarzadeh \* and Genhua Pan

Wolfson Nanomaterials and Devices Laboratory, School of Engineering, Computing and Mathematics, Faculty of Science and Engineering, University of Plymouth, Plymouth PL4 8AA, Devon, UK; g.pan@plymouth.ac.uk

\* Correspondence: mina.safarzadeh@plymouth.ac.uk

**Citation:** Safarzadeh, M.; Pan, G. Detection of a Double-Stranded MGMT Gene Using Electrochemically Reduced Graphene Oxide (ErGO) Electrodes Decorated with AuNPs and Peptide Nucleic Acids (PNA). *Biosensors* **2022**, *12*, 98. <https://doi.org/10.3390/bios12020098>

Academic Editors: Sergey Y. Yurish and Benoît Piro

Received: 10 December 2021

Accepted: 1 February 2022

Published: 5 February 2022

**Publisher's Note:** MDPI stays neutral with regard to jurisdictional claims in published maps and institutional affiliations.



**Copyright:** © 2022 by the authors. Licensee MDPI, Basel, Switzerland. This article is an open access article distributed under the terms and conditions of the Creative Commons Attribution (CC BY) license (<https://creativecommons.org/licenses/by/4.0/>).

**Abstract:** The ability to detect double-stranded DNA (dsDNA) as a biomarker without denaturing it to single-stranded DNA (ss-DNA) continues to be a major challenge. In this work, we report a sandwich biosensor for the detection of the ds-methylated MGMT gene, a potential biomarker for brain tumors and breast cancer. The purpose of this biosensor is to achieve simultaneous recognition of the gene sequence, as well as the presence of methylation. The biosensor is based on reduced graphene oxide (rGO) electrodes decorated with gold nanoparticles (AuNPs) and uses Peptide Nucleic Acid (PNA) that binds to the ds-MGMT gene. The reduction of GO was performed in two ways: electrochemically (ErGO) and thermally (TrGO). XPS and Raman spectroscopy, as well as voltammetry techniques, showed that the ErGO was more efficiently reduced, had a higher C/O ratio, showed a smaller crystallite size of the  $sp^2$  lattice, and was more stable during measurement. It was also revealed that the electro-deposition of the AuNPs was more successful on the ErGO surface due to the higher At% of Au on the ErGO electrode. Therefore, the ErGO/AuNPs electrode was used to develop biosensors to detect the ds-MGMT gene. PNA, which acts as a bio-recognition element, was used to form a self-assembled monolayer (SAM) on the ErGO/AuNPs surface via the amine-AuNPs interaction, recognizing the ds-MGMT gene sequence by its invasion of the double-stranded DNA and the formation of a triple helix. The methylation was then detected using biotinylated-anti-5mC, which was then measured using the amperometric technique. The selectivity study showed that the proposed biosensor was able to distinguish between blank, non-methylated, non-complementary, and target dsDNA spiked in mouse plasma. The LOD was calculated to be 0.86 pM with a wide linear range of 1 pM to 50  $\mu$ M. To the best of our knowledge, this is the first report on using PNA to detect ds-methylated DNA. This sandwich design can be modified to detect other methylated genes, making it a promising platform to detect ds-methylated biomarkers.

**Keywords:** electrochemical reduction of graphene oxide; rGO; PNA; detection of double-stranded DNA; MGMT

## 1. Introduction

DNA methylation is the most exhaustively characterized epigenetic alteration of DNA in which methyl groups ( $CH_3$ ) are covalently bound to DNA. This alteration predominantly happens on cytosines preceding guanines (CpG sites) [1]. The aberrant methylation of the CpG sites has the potential of being a diagnostic, prognostic, and predictive biomarker for various diseases [2,3] including lung cancer [4,5], brain tumors [6], breast cancer [7,8], and prostate cancer [9,10]. The conventional techniques for the detection of DNA methylation are based on bisulfite treatment, methylation-specific PCR (MSP), mass spectrometry (MS), and liquid chromatography (LC), all of which are highly sensitive. However, these techniques have some limitations, such as requiring expensive equipment

and significant sample sizes, as well as specific expertise [11–13]. On the other hand, biosensors have the potential to overcome these limitations due to advantages such as operational simplicity, portability, low cost, and rapid detection. They can either be used on their own or can be combined with conventional techniques to advance the assay specificity and sensitivity. DNA sequencing techniques are another approach for overcoming the limitations of the conventional techniques [11].

Wang et al. [14] developed an electrochemical assay for the detection of circulating methylated DNA based on a sequential discrimination-amplification strategy (SEDA). In this assay, the methylated DNA first underwent a bisulfite modification and then was identified and amplified using asymmetric MSP (AMSP). Finally, it was hybridized with tetrahedral DNA probes that were decorated on a gold electrode. Avidin–HRP was used as the label for amperometric detection. The dynamic range for this assay was reported to be 3–150 pg and the LOD was one methylated DNA molecule in the presence of a 1000-fold excess of unmethylated alleles. Povedano et al. [15] reported an electrochemical platform to detect the four most frequent methylations in DNA and RNA (5mC, 5-hmC, 6mA, and m6A). In this work, the target biomarkers were first captured on protein G-modified MBs (ProtG-MBs) using the corresponding capture antibody for each methylation (anti-5-mC, anti-5-hmC, or anti-m6A/6mA). Subsequently, the amperometric detections were performed using screen-printed electrodes with four carbon working electrodes (SP4CEs) and streptavidin–HRP as the label. The linear ranges were reported to be  $3.9 \times 10^{-4}$ – $1.9 \mu\text{M}$ ,  $2.3 \times 10^{-4}$ – $1.8 \times 10^{-1} \mu\text{M}$ ,  $5.4 \times 10^{-4}$ – $1.1 \times 10^{-1} \mu\text{M}$ ,  $1.7 \times 10^{-5}$ – $3.5 \times 10^{-1} \mu\text{M}$  with LOD of  $3 \times 10^{-5} \mu\text{M}$ ,  $3 \times 10^{-5} \mu\text{M}$ ,  $1 \times 10^{-4} \mu\text{M}$ ,  $9 \times 10^{-7} \mu\text{M}$  for 5-mC, 5-hmC, 6mA, and m6A, respectively. Chen et al. [16] developed an electrochemical biosensor for DNA methylation detection using tetrahedron DNA probes which were anchored to a AuNPs-coated gold electrode with avidin–HRP as the label. This biosensor showed a dynamic range of 1 aM to 1 pM, with the LOD of 0.93 aM.

Peptide Nucleic Acid (PNA) is an artificially synthesized nucleic acid analogue with N-(2-aminoethyl)-glycine motif backbones which are linked together via peptide bonds [17]. PNAs have been used as a bio-recognition element in biosensors as a replacement for DNA-based probes, antibodies, or enzymes to overcome limitations such as denaturation during the assay and steric hindrance caused by large molecules [18]. PNA displays many advantages, including specificity, versatility, and neutral charge, as well as high chemical, biological, and thermal stability. PNA/DNA complexes are shown to be more stable than DNA/DNA systems, with PNA probes being more efficient in hybridization because of its complementary target sequence that leads to an enhanced assay sensitivity [17,19]. Besides superior specificity towards ssDNA and RNA, PNA has shown the ability to specifically target the sequence of dsDNA by strand invasion, forming a triplex structure [20].

Hamidi-Asl et al. [21] reported a PNA-based biosensor for the electrochemical detection of the point mutation of the p53 gene. In this work, first, thiolated PNA probes formed a SAM on a gold electrode surface and then the electrode was incubated in the ds-target gene to form triplex structures. Methylene blue (MB) was used as the label to enhance the electrochemical signal. The linear range was reported to be 10 pM to  $5 \times 10^7$  pM with an LOD of 4.15 pM. Ahmadi and Ahour [22] developed a biosensor based on a graphene oxide modified pencil graphite electrode and PNA to electrochemically detect dsDNA in plasmid samples. GO was first casted on to the pencil graphite electrode and then the PNA probes were immobilized on the modified electrode. Upon incubation of the biosensor in the target ds-DNA, PNA probes detached from the electrode surface, resulting in a guanine oxidation signal, decreasing linearly with the target concentration. Under optimized conditions, the linear range was from 30 pM to 10 nM and the LOD was reported to be 1.3 pM. Ahour et al. [23] reported an electrochemical biosensor for the detection of the double-stranded plasmid (ds-PI) using PNA probes and a gold electrode. The PNA oligomer probes were first immobilized on the surface before capturing the ds-PI target, forming a PNA/ds-PI structure using MB as the label. The dynamic range was from 10 to 300 pg/ $\mu\text{L}$  with an LOD of 9.5 pg/ $\mu\text{L}$ .

In this work, the surface of the working electrode was first drop-coated with GO, followed by a reduction of GO using two different methods (electrochemically and thermally). XPS and Raman spectra showed that ErGO was more efficiently reduced and was more stable using voltammetric measurements than TrGO. After that, AuNPs were electro-deposited on both rGO surfaces. XPS spectra showed that the At% of Au on the ErGO was the highest. SEM and EDS studies confirmed the presence of AuNPs on the ErGO surface. Therefore, the ErGO/AuNPs electrode was used to develop the biosensor assay with the aim of detecting ds-MGMT. Therefore, PNA was used to invade the duplex of the target gene to create a triple helix, after which the methylated sites of the captured ds-MGMT gene were detected using biotinylated-anti-5mC, which were then measured amperometrically using Streptavidin-HRP as the label. The LOD was calculated to be 0.86 pM with a wide linear range, and the developed biosensor showed a high sensitivity in mouse plasma. This biosensor is the first report for the detection of the double-stranded methylated gene, is bisulfite- and PCR-free, and can be tailor-made to detect other methylated genes, which can be beneficial in point-of-care (POC) programs as an inexpensive platform to detect methylated DNA biomarkers.

## 2. Experimental

### 2.1. Materials and Methods

All of the reagents used in this work were of analytical grade. Potassium ferricyanide ( $K_3[Fe(CN)_6]$ ), potassium chloride (KCl), hydroquinone (HQ), hydrogen peroxide solution 30% ( $H_2O_2$ ), Nuclease-Free Water, gold(III) chloride trihydrate ( $HAuCl_4$ ), sulphuric acid ( $H_2SO_4$ ), and 6-Mercapto-1-hexanol (MCH) were purchased from Sigma-Aldrich (Gillingham, UK). Single-layer graphene oxide solution (GO) was ordered from Graphene Supermarket (Ronkonkoma, NY, USA). PNA was obtained from Cambridge Research Biochemicals (Billingham, UK) and its sequence was N-AEEA-AEEA-CACCAAGTCGCAAACGGTGC-C. All other nucleic acids were purchased from Integrated DNA Technologies (Coralville, IA, USA). The ds-MGMT target gene sequences were as follows: GTCCC(M)GAC(M)GCCC(M)GCAGGTCCTC(M)GCGGTGCGCACCGTTTGCGACTTGGTG and CACCAAGTCGCAAACGGTGCGCACCGCGAGGACCTGCGGGCGTCGGGAC, where C(M) was methylcytosine. The non-methylated target sequences were similar to ds-MGMT, with cytosine replacing methylcytosine. The non-complementary target was a methylated three-base mismatch of the target ds-MGMT. Biotinylated anti-5mC and Streptavidin-HRP were ordered from Abcam (Cambridge, UK). Mouse plasma was purchased from Sigma-Aldrich (UK). PBS tablets pH 7.4 were obtained from Fisher Scientific (Loughborough, UK) and the PBS buffer solution was prepared in Milli-Q water.

### 2.2. Apparatus and Measurements

The electrochemical measurements were performed using a  $\mu$ Stat ECL BiPotentiostat/Galvanostat and commercially available screen-printed electrodes (SPE). The working electrodes of the SPEs were made of rGO, the counter electrodes were carbon, and the reference electrodes were silver. The electrodes and BiPotentiostat/Galvanostat were purchased from DropSens (Asturias, Spain).

The CV voltammograms were obtained by cycling the potential between 0.55 and  $-0.2$  V using a scan rate of 50 mV/s in 100  $\mu$ L of 10 mM PBS pH 7.4 solution containing 10 mM  $K_3[Fe(CN)_6]$  and 1 M KCl as electrolyte agents. Amperometric measurements were performed in PBS containing 1 mM HQ under agitation at  $-0.2$  V. Once the background current was stabilized, 0.1 M  $H_2O_2$  solution was added and the current was recorded until the steady-state current was reached. The entire measurement was done in  $\sim 150$  s.

Raman spectra were obtained using an XploRA HORIBA system equipped with an Olympus BX41 microscope and a 532 nm green laser source. The spectra were acquired with a power of 100 mW, a scan range of 1100 to 3000  $cm^{-1}$ , and an exposure time of 5–60 s.

XPS analyses were carried out using a Thermo Scientific Nexsa X-Ray Photoelectron Spectrometer System with a monochromatic Al K $\alpha$ -ray source (1486.68 eV) to obtain the spectra. The pass energy for wide scans was 200 eV with an energy step size of 1 eV and 10 scans. The pass energy for high resolution scans was 40 eV with an energy step size of 0.1 eV and 20 scans. The C/O ratios were calculated using the total At% of C1 peak divided by the total At% of O1s peak obtained from the XPS survey scan for each sample. All of the measurements mentioned above were carried out at room temperature.

### 2.3. Electrode Modification

With the aim of increasing the reproducibility of the SPEs, the electrodes were modified using rGO and AuNPs. The working electrodes were first drop-coated with 0.15 mg/mL of GO aqueous solution and were left to dry at room temperature for 3 h. After that, the GO layers were reduced in two different ways in order to compare the impact of the reduction techniques on the quality of rGO and AuNPs. The electrodes were either reduced electrochemically (ErGO) or thermally (TrGO). The electrochemical reduction of GO was performed using 10 successive CV scans in 10 mM PBS pH 7.4 solution containing 10 mM K<sub>3</sub>[Fe(CN)<sub>6</sub>] and 1 M KCl over a potential range of 0.5 and −1.5 V and a scan rate of 100 mV/S. Thermal reduction was performed at 250 °C for 1 h. After reducing GO, the AuNPs were electro-deposited on both ErGO and TrGO electrodes from 0.5 mM H<sub>2</sub>SO<sub>4</sub> solution containing 1 mM HAuCl<sub>4</sub>, using 5 successive CV cycles over a potential range of 1 and −1 V and a scan rate of 50 mV/s (Figure A1). The electrochemical reduction of GO and electro-deposition of the AuNPs were both performed at room temperature.

### 2.4. Assay Development

Modified electrodes were incubated in 10  $\mu$ M PNA overnight at 4 °C to functionalize a self-assembled monolayer (SAM) on the surface of the working electrodes. On the next day, the electrodes were incubated in 1 mM aqueous solution of MCH for 5 min to minimize the nonspecific binding and then they were incubated in PBS for 1 h to stabilize the SAM. The prepared biosensors were then incubated in various concentrations of dsDNA for 1.5 h at 37 °C, followed by incubation in biotinylated methyl binding antibody for 2 h at room temperature. In order to use the amperometric technique, the biosensors were incubated in diluted Streptavidin-HRP for 30 min prior to the measurements. Various layers of the biosensor are depicted in Figure 1. After each incubation step, the electrodes were rinsed with ultrapure water. All of the incubation steps were carried out in a high humidity chamber.

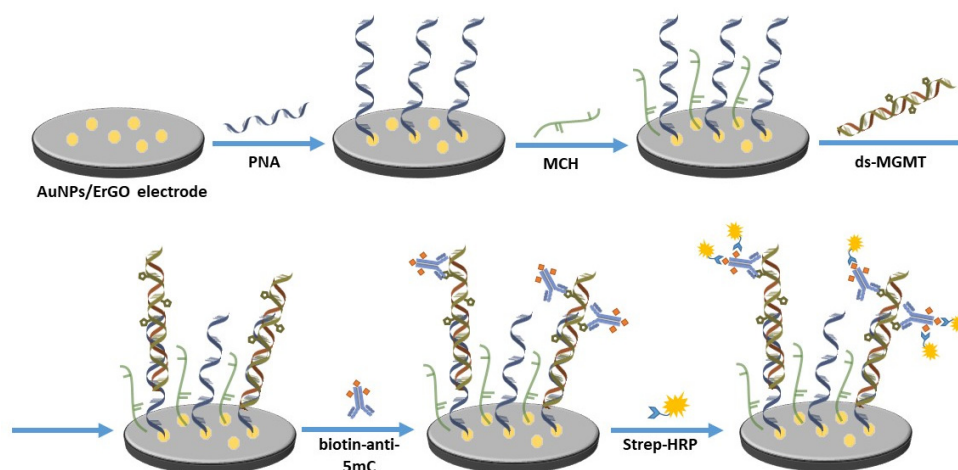


**Figure 1.** A schematic of the developed biosensor. The preparation of the AuNPs/ErGO electrode is depicted in Figure A1.

### 3. Results and Discussion

#### 3.1. GO Reduction

GO-coated electrodes were reduced either electrochemically or thermally in order to achieve a higher reproducibility and quality. The reduction process for both ErGO and TrGO were described in Section 2.3. The reduction degree and the quality of the rGO-modified electrodes were compared using XPS, Raman, and cyclic voltammetry techniques.

The electrochemical reduction of GO was obtained using CV scans for 10 successive cycles. The voltammograms of reducing a GO modified electrode are shown in Figure A2. As can be seen in this figure, a large cathodic peak is located between  $-1.0$  and  $-1.5$  V, disappearing after several cycles. This peak can be attributed to the electrochemical reduction of the functional groups, mainly oxygenated groups which are present at the GO basal plane [24–27]. Therefore, after a few CV cycles, GO was reduced, rGO was obtained, and subsequently, the electric properties improved [28]. The reduction of GO can also be seen from the color change in the working electrode, which changes from black to silver after reduction, consistent with a third-party rGO electrode (Figure A1).

##### 3.1.1. XPS Measurements

XPS measurements were carried out in order to characterize and evaluate the chemical composition of a bare electrode and the GO-, ErGO-, and TrGO-modified electrodes. Wide scans (survey scans) as well as C1s high-resolution scans of all of the samples are shown in Figures 2 and A3 respectively. Table A1 shows a detailed information for all of the peaks observed by the wide scan (Figure 2), their position, FWHM, and At%.

As can be seen in Figure 2, the survey scan spectra of all of the samples show the presence of carbon and oxygen and a trace of contaminants (Na, Cl, S, N), all less than 3% At%. The C/O ratios for the bare, GO, ErGO, and TrGO electrodes were calculated to be 3.97, 2.49, 10.52, and 5.7, respectively. Schniepp et al. [29] reported that in temperatures below  $500$  °C, the C/O ratio only reached 7; however, if the temperature was increased to  $750$  °C, the C/O ratio would rise to more than 13. Ren et al. [30] reported the C/O ratio ranging from 3.1 to 15.1, where the latter was obtained by reducing GO in  $95$  °C for 3 h using hydrazine hydrate as a reducing agent. Yang et al. [31] reported a C/O ratio in the range of 3.09 to 5.38 for the rGO samples that were reduced by adding  $\text{NaBH}_4$  and  $\text{CaCl}_2$  as catalysts and stirring for 12 h at room temperature. Chua et al. [32] increased the C/O ratio from 3.0 to 16.0 by using thiourea dioxide ( $\text{CH}_4\text{N}_2\text{O}_2\text{S}$ ) for 2 to 5 h at  $90$  °C. Although the C/O ratio of the ErGO reported in this study was not as high as the ones reported above, the electrochemical reduction of GO does not require a high temperature or any dangerous reductants. In addition, the reduction process for each electrode took less than 5 min.

Figure A3 shows the high-resolution C1s spectra of bare, GO, ErGO, and TrGO electrodes, where all of the spectra showed asymmetrical shapes. The C1s spectra of the bare electrode (Figure A3A) can be deconvoluted into three component peaks: a C-C peak located at  $284.37$  eV, a C-O peak at  $286.29$  eV, and a C=O peak located at  $288.34$  eV. The C1s spectra of the electrode covered with GO (Figure A3B) can be deconvoluted into a C-C peak located at  $286.43$  eV, a C-O peak at  $284.31$ , and a C=O peak at  $288.01$  eV. The GO sample exhibited the highest amount of oxygen among the samples in both the wide scan and the C1s high-resolution scan. The C1s spectra for ErGO and TrGO exhibited a few tailing peaks. As can be seen in Figure A3C for the ErGO sample, a C-C peak is located at  $284.40$  eV, a C-O peak is at  $285.55$  eV, a C=O peak is at  $288.10$  eV, and a O=C-O peak is located at  $290.49$  eV. Two  $\pi$ - $\pi$  peaks were also observed at  $292.99$  eV and  $295.53$  eV, re-

spectively. The C1s spectra for the TrGO is shown in Figure A3D. The spectra can be deconvoluted into the following peaks: a C-C peak located at 284.29 eV, a C-O peak at 285.84 eV, and a C=O peak at 288.68 eV. A  $\pi$ - $\pi$  peak was also observed at 292.14 eV [33–35].

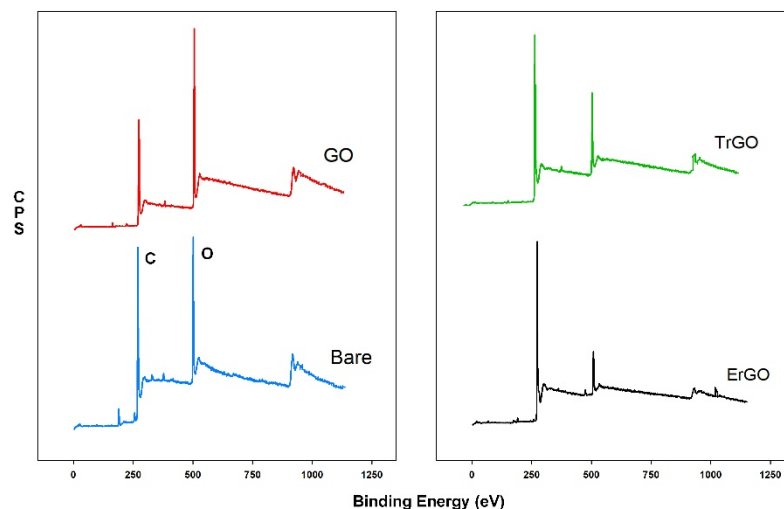


**Figure 2.** XPS wide scan spectra of a bare electrode and GO-, ErGO-, and TrGO-modified electrodes. The C/O ratios of these electrodes were 3.97, 2.49, 10.52, and 5.7, respectively.

### 3.1.2. Raman Spectroscopy

Raman spectroscopy was carried out for a bare electrode and GO, ErGO, and TrGO coated electrodes, and the spectrographs are shown in Figure 3. The peaks at around  $1570\text{ cm}^{-1}$  are G bands which are attributed to in-plane vibrations of the  $\text{sp}^2$ -bonded graphitic carbon atoms. The peaks at  $1350\text{ cm}^{-1}$  are D bands and represent the out-of-plane vibration of the disordered structures [36].  $I_D/I_G$  ratio, or the intensity ratio, is normally used to evaluate disorder level, or the ratio of structural defects in the GO or rGO layers.  $I_D/I_G$  was calculated to be 0.77, 0.88, and 0.89 for bare, GO, and TrGO electrodes, respectively, but 1.15 for ErGO. The higher number in the intensity ratio of ErGO indicates that the reduction process may change the GO structure, resulting in an increase of defects in the structure and a decrease in the average size of the  $\text{sp}^2$  due to the removal of the oxygenated functional groups [37–39]. A 2D band and a D + G band, which become significant in rGO, were also observed at  $2680\text{ cm}^{-1}$  and  $2910\text{ cm}^{-1}$ , respectively, demonstrating the restoration of the graphite structures [39]. The experimental values of the peak locations,  $I_D/I_G$  ratios, and the average crystallite sizes of the  $\text{sp}^2$  lattice ( $L_a$ ) are listed in Table A2. The  $L_a$  values were calculated using the equation  $L_a\text{ (nm)} = (2.4 \times 10^{-10})\lambda_{\text{laser}}^4(I_D/I_G)^{-1}$  for all samples, where  $\lambda_{\text{laser}}$  is the laser wavelength and  $I_D$  and  $I_G$  are the intensities of the D and G Raman bands, respectively [25].

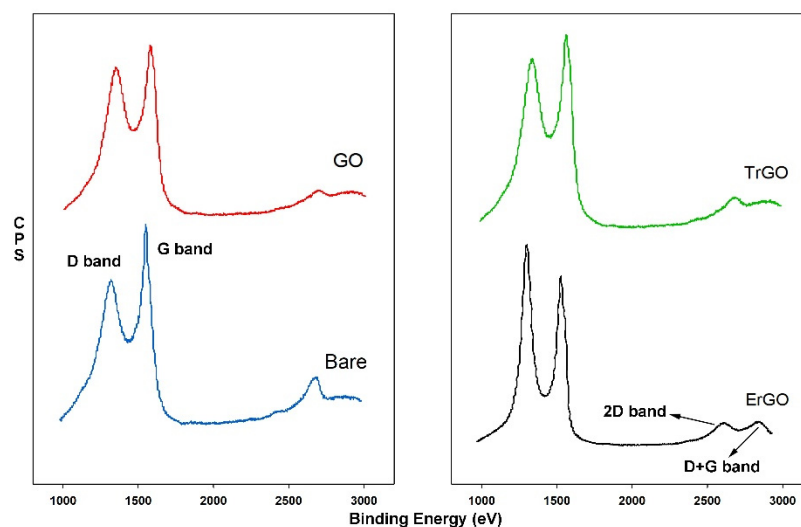


**Figure 3.** Raman spectra obtained from a bare electrode and electrodes modified with GO, ErGO, and TrGO. The  $I_D/I_G$  ratios were 0.77, 0.88, 1.15, and 0.89, respectively.

### 3.1.3. Cyclic Voltammetry

Cyclic voltammetry was used to compare the stability of the electrodes during electrochemical measurements. 10 successive CV scans were performed for a bare electrode, an ErGO-, and a TrGO-modified electrode and the average of the anodic peak currents ( $i_{pa}$ ) of the voltammograms was plotted in Figure A4. As can be seen in this figure, the ErGO reached a higher current compared to both the TrGO and the bare electrodes. For 10 successive measurements, ErGO showed a higher stability and lower fluctuation in the peak currents.

### 3.2. AuNPs

AuNPs were electrochemically deposited on the surface of ErGO- and TrGO-modified electrodes and were characterized using XPS and EDS spectroscopy. SEM was also used to confirm the presence of AuNPs on the surface. The electro-deposition method was described in the experimental section (see Section 2.3). Figure A5 shows the voltammograms of the deposition process in five successive cycles with the potential range of  $-1$  to  $1$  V. As can be seen in this figure, a cathodic peak is located at  $0.1$  V during the first scan, which can be attributed to the reduction of  $Au^{3+}$  ions to Au, as well as the seeding of the AuNPs. This peak has shifted to  $0.5$  V in the next cycles, indicating the easier electro-deposition of gold and the growth of the AuNPs. The Anodic peak at  $0.8$  V can be ascribed to the surface oxidation of the AuNPs [40–42].

### XPS Measurements

Figure 4 shows a wide scan XPS spectra of a bare electrode and the GO-, ErGO-, and TrGO-modified electrodes after the immobilization of the AuNPs. These electrodes are named bare/AuNPs, GO/AuNPs, ErGO/AuNPs, and TrGO/AuNPs, respectively. The bare/AuNPs wide scan spectrum showed two Au4f peaks centered at  $83.83$  eV and  $87.81$  eV and two Au4d peaks at  $334.55$  eV and  $355.27$  eV. A very small peak at  $4.9$  eV was also observed, attributed to Au5d. In the GO/AuNPs spectrum, no peaks related to the AuNPs were observed. However, the ErGO/AuNPs spectrum showed two Au4f peaks at  $94.99$  eV and  $98.87$  eV, respectively, as well as two Au4d peaks located at  $351.1$  eV and  $369.24$  eV. An Au5d and an Au5p were also observed at  $16.7$  eV and  $67.96$  eV, respectively, for this sample. Similarly, in the TrGO/AuNPs spectrum, the Au4f peaks were centered at  $86.79$  eV and  $89.83$  eV, respectively, while the Au4d peaks were observed at  $341.43$  eV and  $359.71$  eV. An Au5d peak was also observed for this sample at  $5.77$  eV. At% of Au for



bare/AuNPs, ErGO/AuNPs, and TrGO/AuNPs were 4.16, 7.38, and 4.08, respectively. This reveals that the ErGO was a better substrate for reducing the AuNPs. Also, the ErGO/AuNPs electrode showed the highest number of AuNPs on the surface, making it the most efficient and promising electrode for further studies. Detailed information about the observed peaks, their positions, the FWHM, and At% is shown in the supplementary information in Table A3.

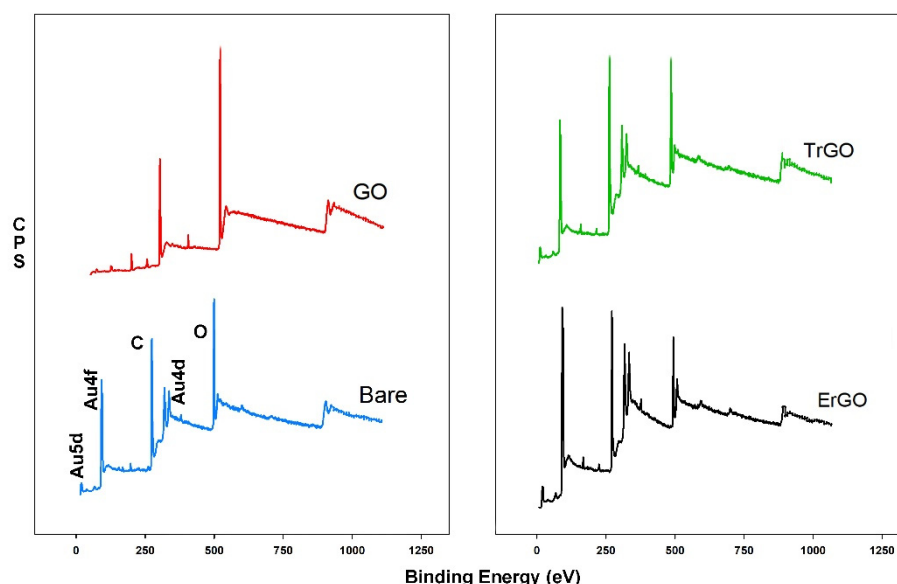


**Figure 4.** XPS spectra of the bare electrode and electrodes modified with GO, ErGO, and TrGO after the deposition of the AuNPs. The ErGO showed the highest At% for Au.

### 3.2.2. SEM and EDS

SEM and EDS were performed to characterize the surface and confirm the presence of gold nanoparticles. Figure A6 shows the SEM images of the ErGO electrode before and after the deposition of the AuNPs on the surface, as well as the EDS spectra of both and the area from which the spectra has been taken. Figure A6A shows the surface of the ErGO electrode exhibiting cracks and wrinkles of 5–20  $\mu\text{m}$ . Figure A6B shows the surface of the ErGO/AuNPs electrode where the AuNPs are homogeneously spread on the surface. The diameter of the nanoparticles is mostly less than 100 nm. EDS spectrographs of the ErGO electrodes before and after the deposition of the AuNPs are shown in Figure A6C,D. The inset tables show the present elements, the relative concentration (Wt%), and the measurement error for each element ( $\sigma$ ). EDS measurements confirm the presence of the AuNPs on the surface.

### 3.3. Assay Development

Electrochemical measurements were used to evaluate the biosensor development steps and the performance of the biosensor. CV scans were performed after each preparation step and amperometric detections were conducted after the biosensors were incubated in various concentrations of ds-methylated-DNA (ds-MGMT). The ErGO/AuNPs-modified electrodes were used as the working electrodes for all of the following experiments.

#### 3.3.1. Optimization

The antigen incubation time and the Streptavidin-HRP concentration for the amperometric measurements were optimized prior to incubating the biosensor in various concentrations (Figure A7).

The antigen incubation time was optimized by incubating at least three electrodes in the ds-methylated DNA for either 0.5, 1, 1.5, or 2 h. The results are displayed in Figure A7A where it is shown that the incubation time of 1.5 h exhibits the highest difference in the current before and after adding the  $\text{H}_2\text{O}_2$ . Consequently, 1.5 h was chosen as the optimized incubation time for the antigen incubation.

The Streptavidin-HRP concentration was optimized by varying its concentration in PBS. The tested concentrations were 0.2%, 0.4%, and 0.6%, and at least three electrodes were incubated in either of these concentrations for 30 min at room temperature prior to the amperometric measurements. As can be seen in Figure A7B, the 0.4% concentration showed the highest difference in the current before and after adding the  $\text{H}_2\text{O}_2$ . Therefore, 0.4% was chosen as the optimized Streptavidin-HRP concentration and was used in further experiments.

### 3.3.2. Cyclic Voltammetry

Figure 5a shows the voltammograms of the various preparation steps of the biosensor (Bare, GO, ErGO, AuNPs, PNA, MCH, and ds-MGMT). As can be seen from the voltammograms, the anodic peak current ( $i_{pa}$ ) of the bare electrode was first seen at 57.5  $\mu\text{A}$ . After drop-coating the surface of the working electrode in GO, the  $i_{pa}$  decreased to 1.05  $\mu\text{A}$  due to the non-conductive nature of GO [43]. After the electrochemical reduction of GO, the  $i_{pa}$  increased to 117.5  $\mu\text{A}$ . This increase is due to the electrochemical reduction of GO and the production of rGO. rGO is electrically conductive and has a high concentration of charge carriers, mobility, and a high number of available electroactive sites on the surface, facilitating electron transfer [44,45]. After the electrochemical reduction of GO, the  $i_{pa}$  decreased to 107.2  $\mu\text{A}$  by reducing the AuNPs on the rGO surface, followed by a further decrease to 73.6  $\mu\text{A}$  after overnight incubation in PNA, confirming the immobilization of the AuNPs and PNA on the surface, respectively. Amine groups (N-terminal of PNA) are able to self-assemble on the AuNPs and form a SAM, decreasing the electron transfer between the electrode and the electrolyte [46,47]. The  $i_{pa}$  decreased once more to 63.7  $\mu\text{A}$  after blocking the surface to decrease the chance of non-specific bonding. Finally, the  $i_{pa}$  slightly increased to 68.2  $\mu\text{A}$  after the electrode was incubated in target ds-MGMT nucleotides, confirming the presence of the dsDNA on the surface. The dsDNA was captured by the strand invasion of PNA towards the DNA/DNA duplex and the formation of a triple helix [48,49]. Additionally, after the reduction of GO, the peak potential first shifted positively towards higher potentials, followed by a negative shift after the deposition of the AuNPs. Furthermore, a small positive shift in the peak potential was observed after the immobilization of PNA, MCH, and triple formation, which might be due to the spatial blockage and hindered electron transfer on the surface [50].

The cathodic peak currents ( $i_{pc}$ ) of the CV voltammograms showed the same trend as the anodic peak current after each incubation step, with corresponding positive and negative shifts.

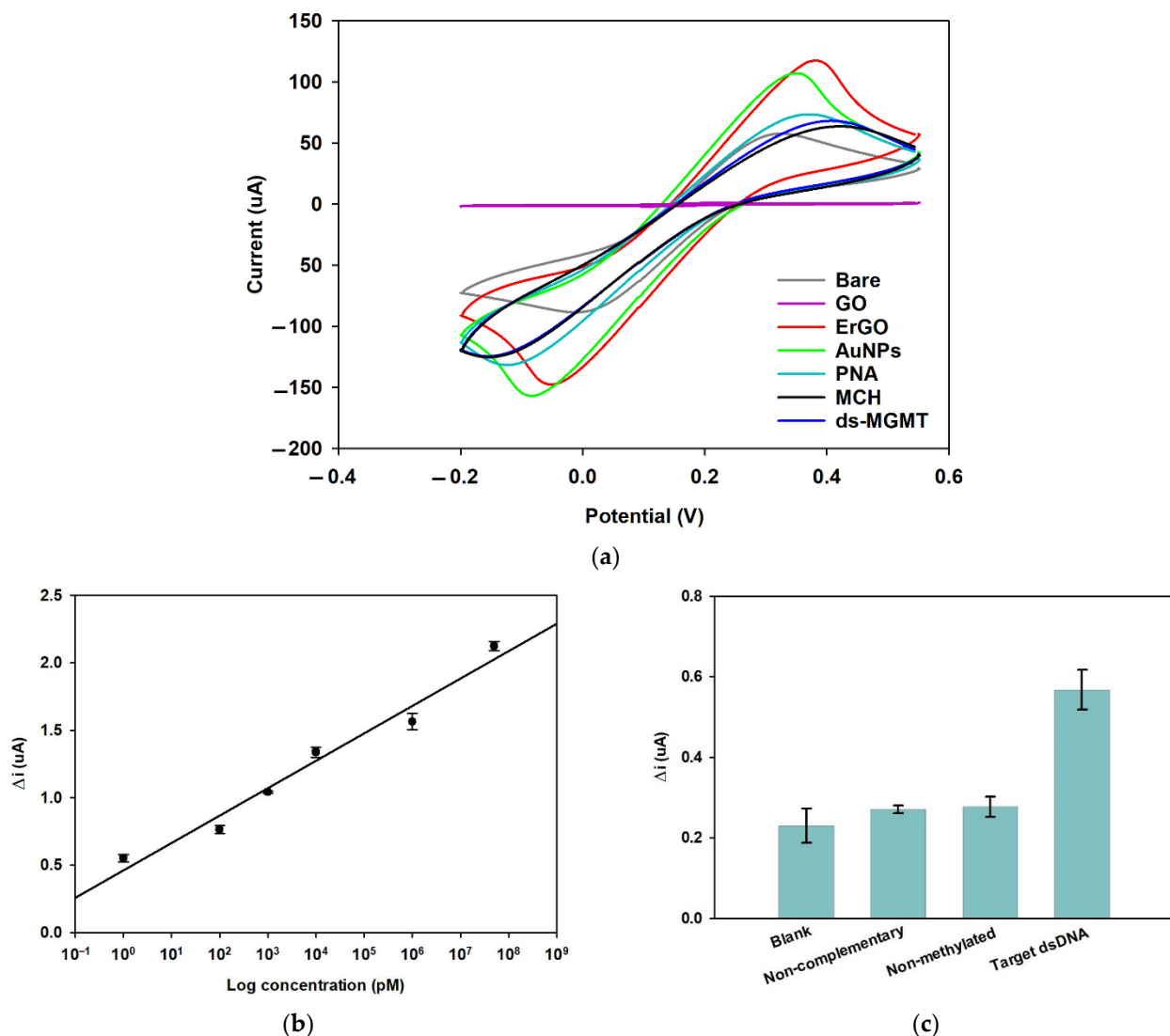


**Figure 5.** Comparison of CV voltammograms of the various preparation steps of the biosensor: Bare, GO, ErGO, AuNPs, PNA, MCH, and ds-MGMT (a). Linear regression studies for the ds-MGMT gene using the amperometric technique. Error bars are the standard deviation of at least three electrodes (b). Comparison of the amperometric response of the biosensor in different targets: blank (mouse plasma), the ss-MGMT gene, and the ds-MGMT gene spiked in mouse plasma (c).

### 3.3.3. Linear Regression

Amperometric detection was used to perform the linear regression studies. As explained in Section 2.4, after the biosensor was incubated in Streptavidin-HRP for 30 min, the amperometric measurements were first performed in the HQ solution for measuring the background signal, followed by the addition of  $H_2O_2$  and the measurement of the reduction of the HRP labels. The difference between the background signal and the signal from the HRP reduction ( $\Delta i$ ) was plotted as a logarithmic function of the concentration in Figure 5b. As can be seen in this figure, the difference in the current increases with an increase in the concentration due to the presence of more HRP labels; this is correlated with the presence of more ds-MGMT nucleotides. The best fit linear model is  $y = 0.46 \ln(x) + 0.20$ , with  $R^2 = 0.96$  with the linear range of 1 pM to 50  $\mu$ M. The LOD was calculated to be 0.86 pM using the equation  $LOD = 3.3\sigma/m$ , where  $\sigma$  is the standard deviation of the amperometric responses of four blank samples and  $m$  is the slope of the calibration curve.

### 3.3.4. Selectivity

The selectivity study was performed with 100 pM of target dsDNA (ds-MGMT) non-complementary as well as non-methylated oligonucleotides spiked in mouse plasma and a blank mouse plasma sample. As can be seen in Figure 5c, there was a significant difference in the responses of the blank and the ds-MGMT samples. Also, the fabricated sensor was able to distinguish between the same concentration of target DNA and the non-complementary and non-methylated DNAs. The higher response of the target DNA means that the biosensor has successfully captured the target DNA, the antibodies have identified the methylated sites on the target DNA, and the reduction of HRP has taken place as described in Section 3.3.3.

### 3.3.5. Comparison with other Works

In Table 1, the various parameters of the proposed biosensor, including the working electrode, the bioreceptor, the dynamic range, the LOD, and the measurement techniques, are compared with other electrochemical biosensors so far reported for the detection of DNA methylation. Although most of the works summarized in Table 1 report a better LOD than the results in this work, they all detect single-stranded DNA (ssDNA). In addition, some of the reported biosensors only detect the presence of methylation, insensitive to the gene sequence, while in this work, the presence of the methylation and the sequence of the double-stranded target gene are detected simultaneously.

**Table 1.** A comparison with other biosensing assays to detect methylated DNA.

Electrode	Bioreceptor	Dynamic Range/LOD	Technique	Reference
Gold modified with gold nanoparticles	stem-loop-tetrahedron composite DNA	$10^{-6} - 10$ pM $9.326 \times 10^{-7}$ pM	Chronoamperometry	[16]
SPCE and immuno-magnetic beads (MBs)	Anti-5mC	$4 - 2.5 \times 10^2$ pM 1 pM	Amperometry	[51]
MoS <sub>2</sub> Nanosheets	FAM-labeled probe DNA	$100 - 2 \times 10^5$ pM 140 pM	Fluorescence	[52]
SPCE modified with rGO and polyvinyl alcohol	Anti-5mC immobilized and DNA probe conjugated with Fe <sub>3</sub> O <sub>4</sub> -citric acid nanocomposites	$7 \times 10^{-4} - 140.29$ pM $6.31 \times 10^{-4}$ pM	DPV/EIS	Coralville, Iowa [53]
rGO modified with ammonium hydroxide	Anti-5mC and complementary DNA	0.5 – 100 pM 0.012 pM	DPV	[36]
AuNPs/ErGO	PNA and anti-5mC	$1 - 5 \times 10^7$ pM 0.86 pM	Amperometry	This work

## 4. Conclusions

A biosensor for the detection of the ds-MGMT gene has been developed in this work using an ErGO/AuNPs-modified electrode. The electrochemical and thermal reductions

of GO were also compared. A high C/O ratio was achieved using electrochemical reduction of GO without using any harmful reductants and in a shorter period of time compared to the techniques reported in other papers. The  $I_D/I_G$  ratios showed higher numbers of defect sites and a smaller crystallite size of  $sp^2$  structures in ErGO. After the electro-deposition of the AuNPs, the At% of gold for the ErGO/AuNPs was higher compared to the TrGO/AuNPs. Therefore, the ErGO/AuNPs electrode was used as the base electrode to develop the biosensor. PNA was used to form a SAM layer on the surface via the amine-AuNPs interaction where PNA acts as the bio-recognition element. The linear range was 1 pM to 50  $\mu$ M and the LOD was calculated to be 0.86 pM without any PCR amplification or bisulfite treatment. Selectivity studies showed that the biosensor is able to distinguish between blank mouse plasma, the target dsDNA, and the non-complementary and non-methylated oligonucleotides spiked in mouse plasma. To the best of our knowledge, this is the first report on using PNA to detect methylated DNA and to capture double-stranded methylated DNA. The sandwich design can be tailor-made to detect other methylated genes, revealing it as basis for clinical applications in diagnostics and a marking it as promising platform for detecting ds-methylated biomarkers.

**Author Contributions:** Conceptualization, methodology, validation, formal analysis, investigation, data curation, writing—original draft preparation, writing—review and editing, and visualization, M.S.; writing—review and editing, supervision, and funding acquisition, G.P. All authors have read and agreed to the published version of the manuscript.

**Funding:** This research was funded by EU Horizon 2020, Marie Skłodowska-Curie Actions-ITN-ETN AiPBAND grant number 764281. (Start date: 1 January 2018. End date: 30 June 2022) <https://www.aipband-itn.eu/>.

**Institutional Review Board Statement:** Not applicable

**Informed Consent Statement:** Not applicable.

**Data Availability Statement:** The data that support the findings of this study are available upon reasonable request from the corresponding author.

**Acknowledgments:** Scanning electron microscopy was performed by the Plymouth Electron Microscopy Centre (PEMC). The x-ray photoelectron (XPS) data collection was performed at the EPSRC National Facility for XPS ("HarwellXPS"), operated by Cardiff University and UCL, under Contract No. PR16195.

**Conflicts of Interest:** The authors declare no conflict of interest.

## Appendix A

### *Appendix A.1. Experimental*

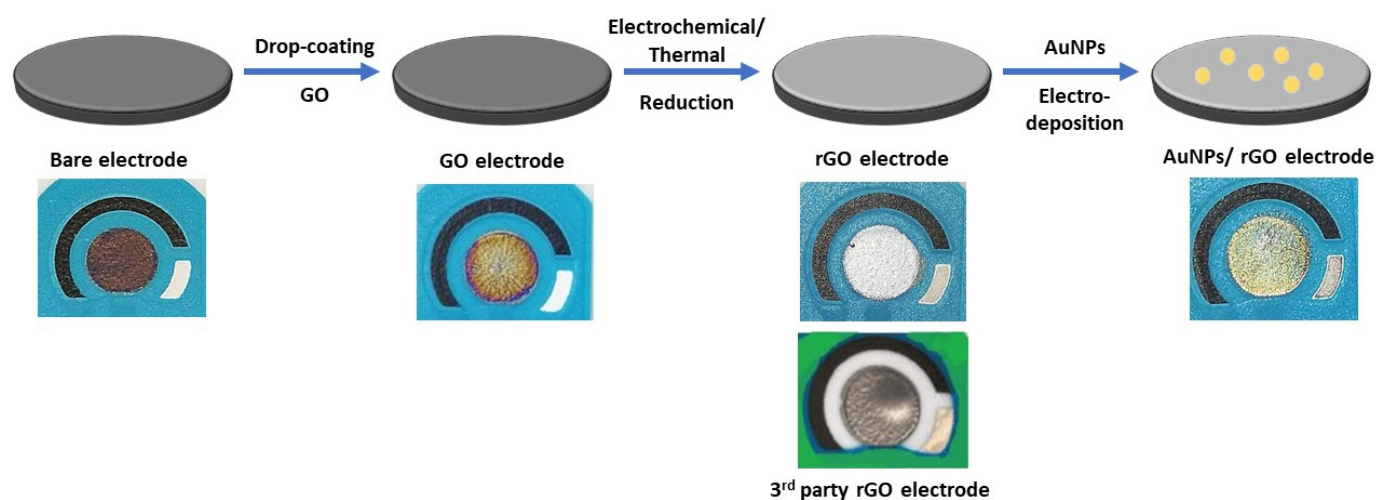


**Figure A1.** A schematic of the surface modification procedure of a screen-printed electrode (Section 2.3) and the changes to the appearance of the working electrode.

## Appendix A.2. Results and Discussion

### Appendix A.2.1. GO Reduction

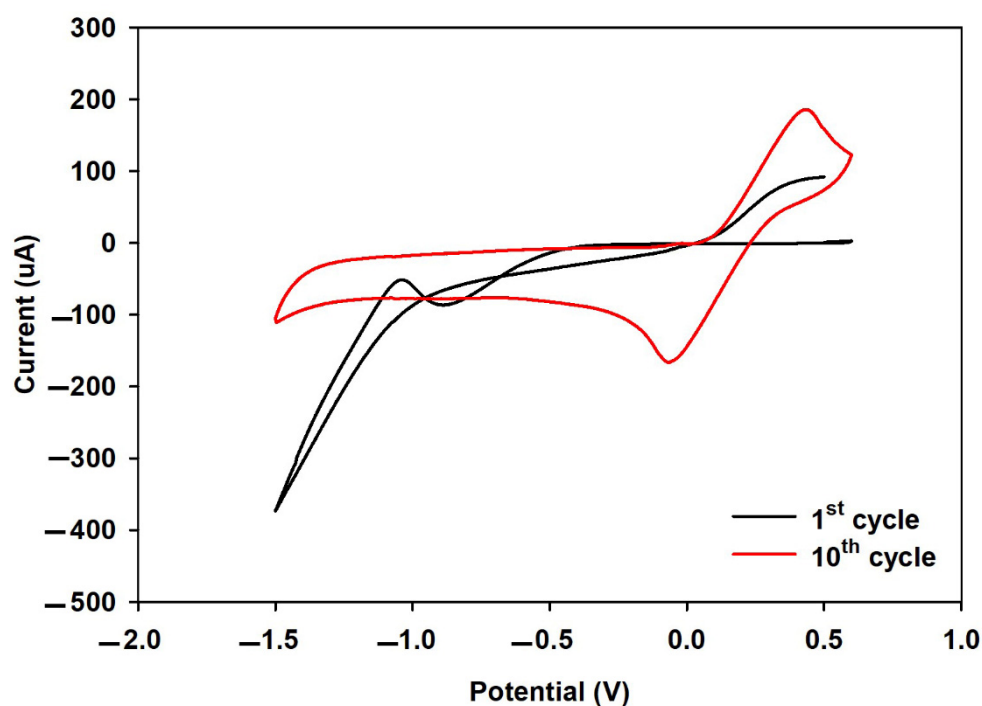
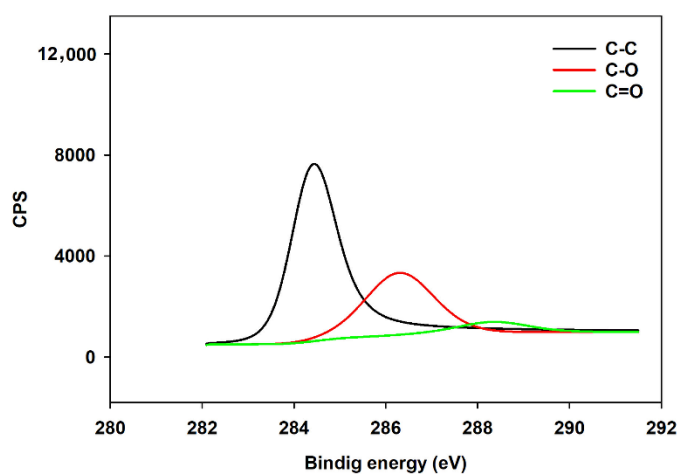


**Figure A2.** The voltammograms of the CV cycles used to electrochemically reduce GO.

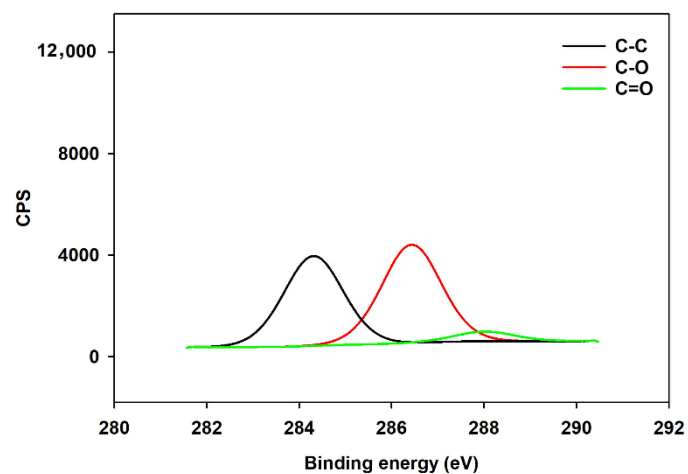
### Appendix A.2.2. XPS

**Table A1.** Detailed information of the XPS peaks, their positions, the FWHM, and the At% for a bare electrode and for the electrodes modified with GO, ErGO, and TrGO. These data are obtained from the XPS survey scans (Figure 2).

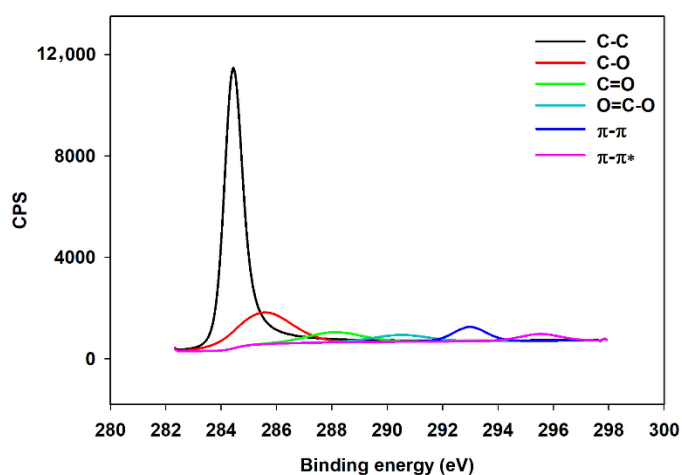
Sample	Peak Name	Position	FWHM	At%
Bare	O1s	532.10	3.31	19.26
	C1s	285.10	3.77	76.49
	N1s	400.10	3.10	1.37
	Cl2p	200.10	3.32	2.87
GO	O1s	534.37	3.01	27.98
	C1s	287.37	4.50	69.63
	N1s	402.37	3.34	1.30
	S2p	168.37	3.07	1.10
ErGO	O1s	533.33	3.89	8.57
	C1s	285.33	2.73	90.15
	Na1s	1074.33	2.87	0.44
	Cl2p	199.33	3.48	0.85
TrGO	O1s	565.37	3.88	14.65
	C1s	312.37	3.06	83.57
	N1s	430.37	3.77	1.31
	Cl2p	194.37	3.16	0.47



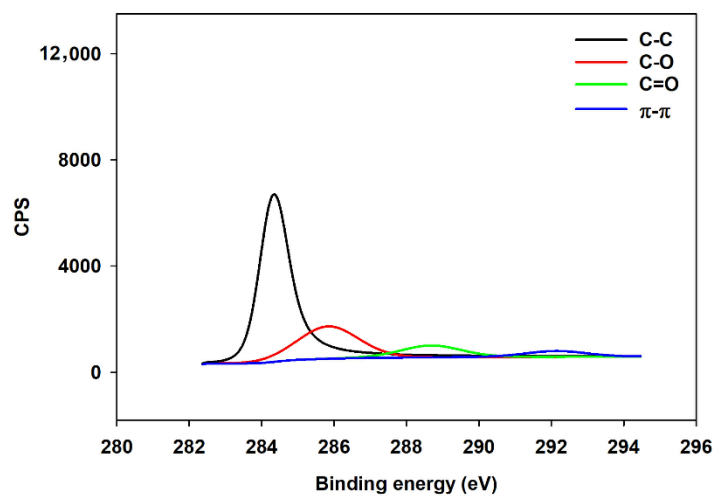
(A)



(B)



(C)



(D)

**Figure A3.** The C1s high resolution spectra of a bare electrode (A) and GO-(B), ErGO-(C), and TrGO-(D) modified electrodes.

#### Appendix A.2.3. Raman

**Table A2.** The experimental values of the peak locations,  $I_D/I_G$  ratios, and the average crystallite sizes of the  $sp^2$  lattice ( $L_a$ ) of all samples.

Sample	D Peak Location	G Peak Location	$I_D/I_G$	$L_a$ (nm)
	( $\text{cm}^{-1}$ )	( $\text{cm}^{-1}$ )		
Bare	1340	1570	0.77	24.99
GO	1350	1570	0.88	21.84
TrGO	1340	1570	0.89	21.60
ErGO	1350	1570	1.15	16.72

#### Appendix A.2.4. Cyclic Voltammetry



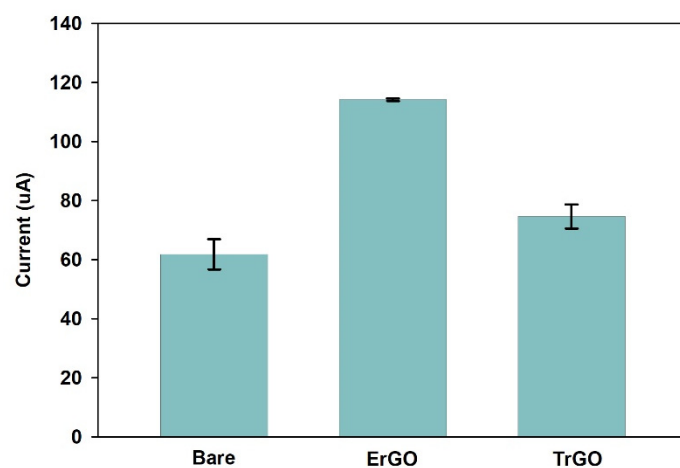


**Figure A4.** The anodic peak currents ( $I_{pa}$ ) of 10 successive cycles of CV voltammograms of a bare electrode and electrodes modified with ErGO and TrGO.

#### Appendix A.2.5. AuNPs

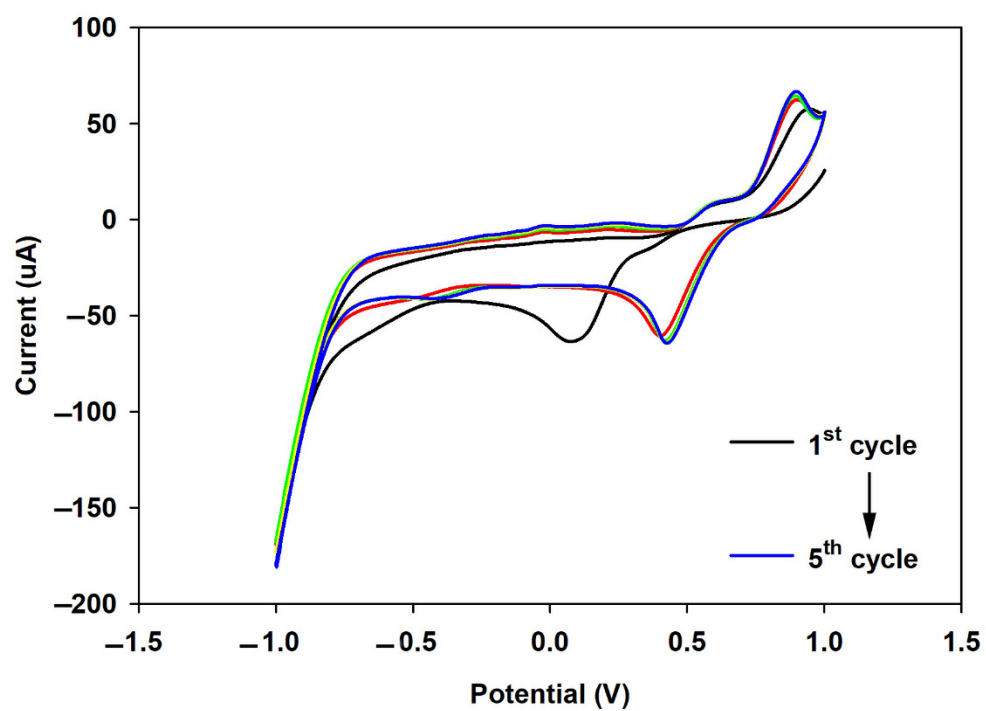


**Figure A5.** The voltammograms of five successive CV cycles used to deposit AuNPs.

#### Appendix A.2.6. SEM and EDS

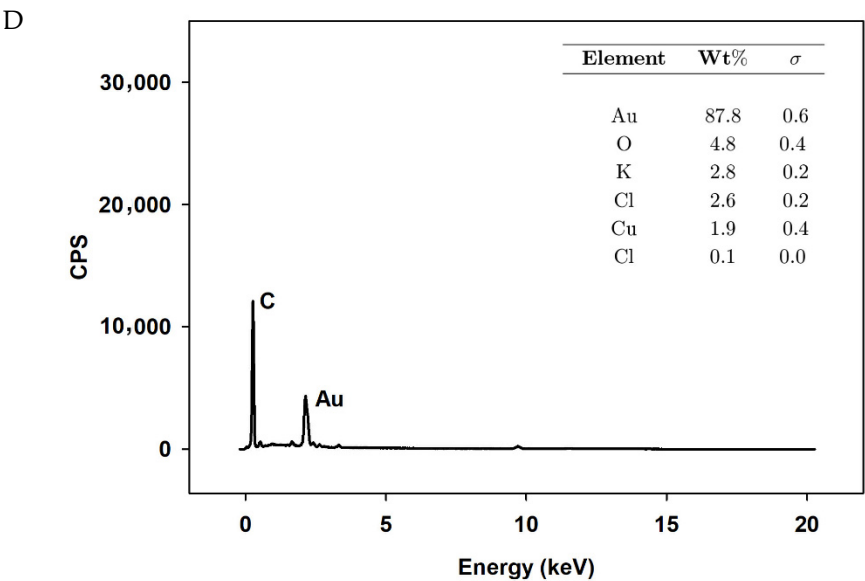
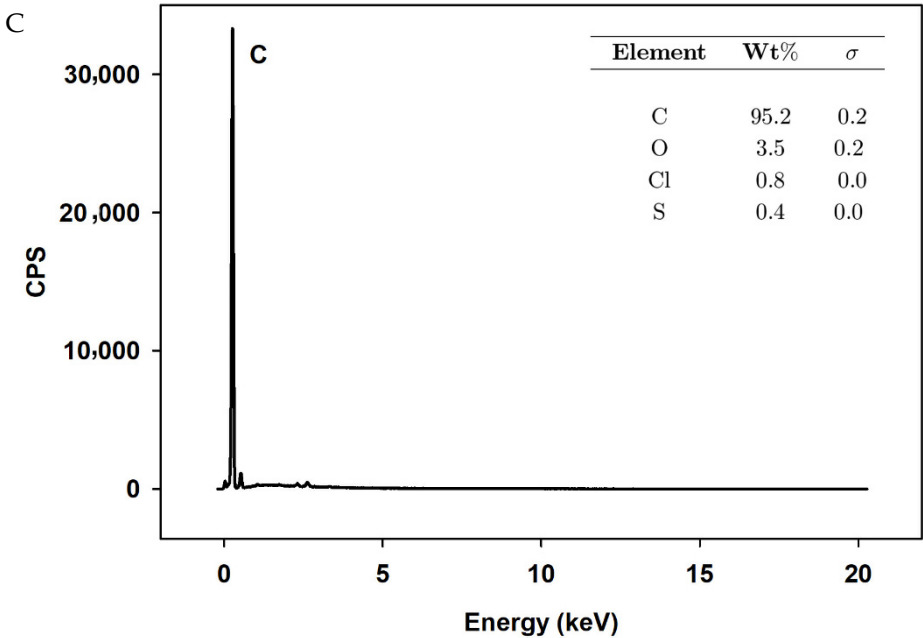
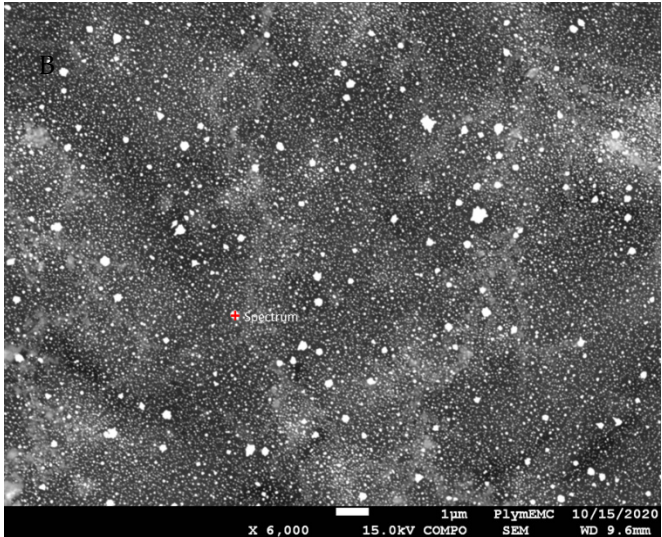
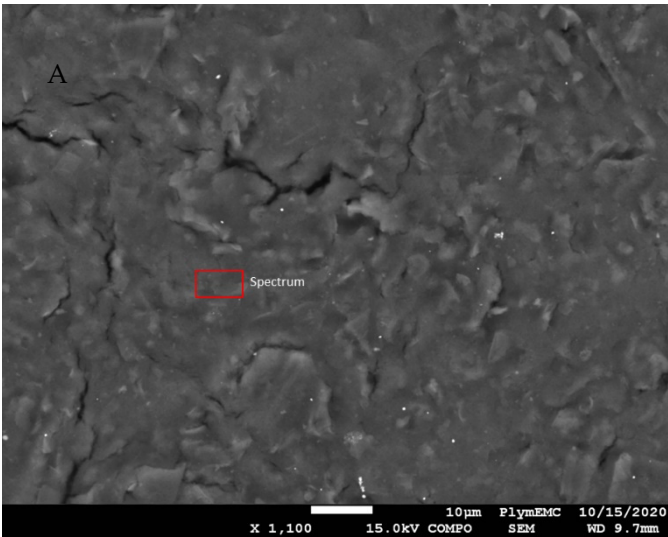


**Figure A6.** SEM images of ErGO (A) and ErGO/AuNPs (B) electrodes. EDS spectra of the ErGO (C) and ErGO/AuNPs (D) electrodes. The inset tables show the present elements, the relative concentration (Wt%) of each element, and their measurement errors ( $\sigma$ ).

### Appendix A.2.7. XPS

**Table A3.** Detailed information for the XPS peaks, their position, the FWHM, and the At% for a bare electrode after the deposition of the AuNPs and electrodes modified with GO/AuNPs, ErGO/AuNPs, and TrGO/AuNPs. These data are obtained from XPS survey scans (Figure 4).

Sample	Peak Name	Position	FWHM	At%
Bare/AuNPs	O1s	532.83	3.20	19.97
	C1s	284.83	3.61	72.11
	N1s	401.83	3.27	1.56
	Cl2p	199.83	3.37	1.50
	S2p	168.83	3.25	0.71
	Au4f	83.83	2.50	4.16
GO/AuNPs	O1s	531.89	3.00	29.40
	C1s	284.89	4.26	63.83
	N1s	400.89	2.84	2.76
	S2p	168.89	3.01	4.00
ErGO/AuNPs	O1s	551.00	3.26	13.25
	C1s	289.99	2.77	74.10
	N1s	418.99	3.09	2.89
	S2p	180.99	2.97	2.38
	Au4f	94.99	2.80	7.38
TrGO/AuNPs	O1s	542.79	3.43	17.65
	C1s	298.79	2.99	75.06
	N1s	408.79	3.43	1.75
	S2p	171.79	2.96	1.46
	Au4f	86.79	2.43	4.08

## Appendix A.2.8. Optimization

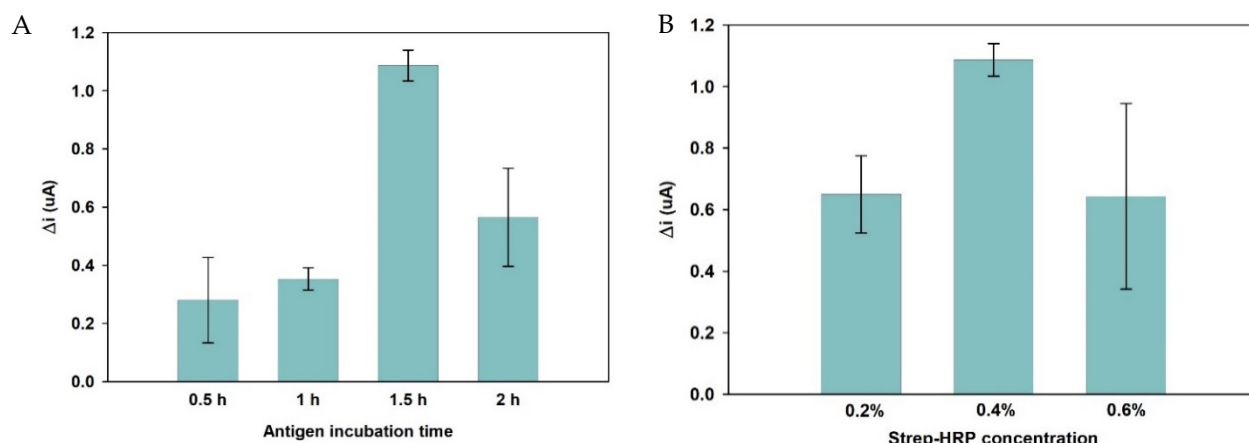


**Figure A7.** The results of the optimization studies. The incubation time for the optimizing antigen (ds-MGMT) (A) and the Streptavidin-HRP concentration (B).

## References

- Lam, K.; Pan, K.; Linnekamp, J.F.; Medema, J.P.; Kandimalla, R. DNA methylation-based biomarkers in colorectal cancer: A systematic review. *Biochim. Biophys. Acta Rev. Cancer* **2016**, *1866*, 106–120.
- Mikeska, T.; Craig, J.M. DNA methylation biomarkers: Cancer and beyond. *Genes* **2014**, *5*, 821–864.
- Das, P.M.; Singal, R. DNA methylation and cancer. *J. Clin. Oncol.* **2004**, *22*, 4632–4642.
- Usadel, H.; Brabender, J.; Danenberg, K.D.; Jerónimo, C.; Harden, S.; Engles, J.; Danenberg, P.V.; Yang, S.; Sidransky, D. Quantitative adenomatous polyposis coli promoter methylation analysis in tumor tissue, serum, and plasma DNA of patients with lung cancer. *Cancer Res.* **2002**, *62*, 371–375.
- Kersting, M.; Friedl, C.; Kraus, A.; Behn, M.; Pankow, W.; Schuermann, M. Differential frequencies of p16INK4a promoter hypermethylation, p53 mutation, and K-ras mutation in exfoliative material mark the development of lung cancer in symptomatic chronic smokers. *J. Clin. Oncol.* **2000**, *18*, 3221–3229.
- Esteller, M.; Garcia-Foncillas, J.; Andion, E.; Goodman, S.N.; Hidalgo, O.F.; Vanaclocha, V.; Baylin, S.B.; Herman, J.G. Inactivation of the DNA-repair gene MGMT and the clinical response of gliomas to alkylating agents. *New Engl. J. Med.* **2000**, *343*, 1350–1354.
- Silva, J.M.; Dominguez, G.; Garcia, J.M.; Gonzalez, R.; Villanueva, M.J.; Navarro, F.; Provencio, M.; San Martin, S.; Espana, P.; Bonilla, F. Presence of tumor DNA in plasma of breast cancer patients: Clinicopathological correlations. *Cancer Res.* **1999**, *59*, 3251–3256.
- Evron, E.; Dooley, W.C.; Umbricht, C.B.; Rosenthal, D.; Sacchi, N.; Gabrielson, E.; Soito, A.B.; Hung, D.T.; Ljung, B.M.; Davidson, N.E.; et al. Detection of breast cancer cells in ductal lavage fluid by methylation-specific PCR. *Lancet* **2001**, *357*, 1335–1336.
- Goessl, C.; Krause, H.; Müller, M.; Heicappell, R.; Schrader, M.; Sachsinger, J.; Miller, K. Fluorescent methylation-specific polymerase chain reaction for DNA-based detection of prostate cancer in bodily fluids. *Cancer Res.* **2000**, *60*, 5941–5945.
- Lee, W.H.; Morton, R.A.; Epstein, J.I.; Brooks, J.D.; Campbell, P.A.; Bova, G.S.; Hsieh, W.S.; Isaacs, W.B.; Nelson, W.G. Cytidine methylation of regulatory sequences near the pi-class glutathione S-transferase gene accompanies human prostatic carcinogenesis. *Proc. Natl. Acad. Sci. USA* **1994**, *91*, 11733–11737.
- Bhattacharjee, R.; Moriam, S.; Umer, M.; Nguyen, N.T.; Shiddiky, M.J. DNA methylation detection: Recent developments in bisulfite free electrochemical and optical approaches. *Analyst* **2018**, *143*, 4802–4818.
- Kurdyukov, S.; Bullock, M. DNA methylation analysis: Choosing the right method. *Biology* **2016**, *5*, 3.
- Shanmuganathan, R.; Basheer, N.B.; Amirthalingam, L.; Muthukumar, H.; Kaliaperumal, R.; Shanmugam, K. Conventional and nanotechniques for DNA methylation profiling. *J. Mol. Diagn.* **2013**, *15*, 17–26.
- Wang, X.; Chen, F.; Zhang, D.; Zhao, Y.; Wei, J.; Wang, L.; Song, S.; Fan, C.; Zhao, Y. Single copy-sensitive electrochemical assay for circulating methylated DNA in clinical samples with ultrahigh specificity based on a sequential discrimination–amplification strategy. *Chem. Sci.* **2017**, *8*, 4764–4770.
- Povedano, E.; Gamella, M.; Torrente-Rodríguez, R.M.; Montiel, V.R.V.; Montero-Calle, A.; Solís-Fernández, G.; Navarro-Villoslada, F.; Pedrero, M.; Peláez-García, A.; Mendiola, M.; et al. Multiplexed magnetic beads-assisted amperometric bioplatfroms for global detection of methylations in nucleic acids. *Anal. Chim. Acta* **2021**, *1182*, 338946.
- Chen, X.; Huang, J.; Zhang, S.; Mo, F.; Su, S.; Li, Y.; Fang, L.; Deng, J.; Huang, H.; Luo, Z.; et al. Electrochemical biosensor for DNA methylation detection through hybridization chain-amplified reaction coupled with a tetrahedral DNA nanostructure. *ACS Appl. Mater. Interfaces* **2019**, *11*, 3745–3752.
- D'Agata, R.; Giuffrida, M.C.; Spoto, G. Peptide nucleic acid-based biosensors for cancer diagnosis. *Molecules* **2017**, *22*, 1951.

18. Puiu, M.; Bala, C. Peptide-based electrochemical biosensors. In *Electrochemical Biosensors*; Elsevier: Amsterdam, The Netherlands, 2019; pp. 277–306.
19. Karimzadeh, A.; Hasanazadeh, M.; Shadjou, N.; de la Guardia, M. Peptide based biosensors. *Trends Anal. Chem.* **2018**, *107*, 1–20.
20. Baker, E.S.; Hong, J.W.; Gaylord, B.S.; Bazan, G.C.; Bowers, M.T. PNA/dsDNA complexes: Site specific binding and dsDNA biosensor applications. *J. Am. Chem. Soc.* **2006**, *128*, 8484–8492.
21. Hamidi-Asl, E.; Raoof, J.B.; Ojani, R.; Golabi, S.M.; Hejazi, M.S. A new peptide nucleotide acid biosensor for electrochemical detection of single nucleotide polymorphism in duplex DNA via triplex structure formation. *J. Iran. Chem. Soc.* **2013**, *10*, 1075–1083.
22. Ahmadi, M.; Ahour, F. An electrochemical biosensor based on a graphene oxide modified pencil graphite electrode for direct detection and discrimination of double-stranded DNA sequences. *Anal. Methods* **2020**, *12*, 4541–4550.
23. Ahour, F.; Pournaghi-Azar, M.H.; Alipour, E.; Hejazi, M.S. Detection and discrimination of recombinant plasmid encoding hepatitis C virus core/E1 gene based on PNA and double-stranded DNA hybridization. *Biosens. Bioelectron.* **2013**, *45*, 287–291.
24. Wang, Z.; Zhou, X.; Zhang, J.; Boey, F.; Zhang, H. Direct electrochemical reduction of single layer graphene oxide and subsequent functionalization with glucose oxidase. *J. Phys. Chem. C* **2009**, *113*, 14071–14075.
25. Marrani, A.G.; Motta, A.; Palmieri, V.; Perini, G.; Papi, M.; Dalchiele, E.A.; Schrebler, R.; Zanon, R. A comparative experimental and theoretical study of the mechanism of graphene oxide mild reduction by ascorbic acid and N-acetyl cysteine for biomedical applications. *Mater. Adv.* **2020**, *1*, 2745–2754.
26. Devadas, B.; Madhu, R.; Chen, S.M.; Yeh, H.T. Controlled electrochemical synthesis of new rare earth metal lutetium hexacyanoferrate on reduced graphene oxide and its application as a salicylic acid sensor. *J. Mater. Chem. B* **2014**, *2*, 7515–7523.
27. Devadas, B.; Rajkumar, M.; Chen, S.M.; Saraswathi, R. Electrochemically reduced graphene oxide/neodymium hexacyanoferrate modified electrodes for the electrochemical detection of paracetamol. *Int. J. Electrochem. Sci.* **2012**, *7*, 3339–3349.
28. Wu, B.; Zhao, N.; Hou, S.; Zhang, C. Electrochemical synthesis of polypyrrole, reduced graphene oxide, and gold nanoparticles composite and its application to hydrogen peroxide biosensor. *Nanomaterials* **2016**, *6*, 220.
29. Schniepp, H.C.; Li, J.L.; McAllister, M.J.; Sai, H.; Herrera-Alonso, M.; Adamson, D.H.; Prud'homme, R.K.; Car, R.; Saville, D.A.; Aksay, I.A. Functionalized single graphene sheets derived from splitting graphite oxide. *J. Phys. Chem. B* **2006**, *110*, 8535–8539.
30. Ren, P.G.; Yan, D.X.; Ji, X.; Chen, T.; Li, Z.M. Temperature dependence of graphene oxide reduced by hydrazine hydrate. *Nanotechnology* **2010**, *22*, 055705.
31. Yang, Z.Z.; Zheng, Q.B.; Qiu, H.X.; Jing, L.; Yang, J.H. A simple method for the reduction of graphene oxide by sodium borohydride with CaCl<sub>2</sub> as a catalyst. *New Carbon Mater.* **2015**, *30*, 41–47.
32. Chua, C.K.; Ambrosi, A.; Pumera, M. Graphene oxide reduction by standard industrial reducing agent: Thiourea dioxide. *J. Mater. Chem.* **2012**, *22*, 11054–11061.
33. Al-Gaashani, R.; Najjar, A.; Zakaria, Y.; Mansour, S.; Atieh, M. XPS and structural studies of high-quality graphene oxide and reduced graphene oxide prepared by different chemical oxidation methods. *Ceram. Int.* **2019**, *45*, 14439–14448.
34. Yang, D.; Velamakanni, A.; Bozoklu, G.; Park, S.; Stoller, M.; Piner, R.D.; Stankovich, S.; Jung, I.; Field, D.A.; Ventrone, C.A., Jr.; et al. Chemical analysis of graphene oxide films after heat and chemical treatments by X-ray photoelectron and Micro-Raman spectroscopy. *Carbon* **2009**, *47*, 145–152.
35. Krishnamoorthy, K.; Veerapandian, M.; Yun, K.; Kim, S.J. The chemical and structural analysis of graphene oxide with different degrees of oxidation. *Carbon* **2013**, *53*, 38–49.
36. Safarzadeh, M.; Suhail, A.; Sethi, J.; Sattar, A.; Jenkins, D.; Pan, G. A Label-Free DNA-Immunosensor Based on Aminated rGO Electrode for the Quantification of DNA Methylation. *Nanomaterials* **2021**, *11*, 985.
37. Lee, C.S.; Yu, S.H.; Kim, T.H. One-step electrochemical fabrication of reduced graphene oxide/gold nanoparticles nanocomposite-modified electrode for simultaneous detection of dopamine, ascorbic acid, and uric acid. *Nanomaterials* **2018**, *8*, 17.
38. Le, V.H.; Nguyen, T.H.; Nguyen, H.H.; Huynh, L.T.N.; Vo, A.L.; Nguyen, T.K.T.; Nguyen, D.T.; Lam, V.Q. Fabrication and electrochemical behavior investigation of a Pt-loaded reduced graphene oxide composite (Pt@ rGO) as a High-performance cathode for dye-sensitized solar cells. *Int. J. Photoenergy* **2020**, <https://doi.org/10.1155/2020/8927124>
39. Wu, J.B.; Lin, M.L.; Cong, X.; Liu, H.N.; Tan, P.H. Raman spectroscopy of graphene-based materials and its applications in related devices. *Chem. Soc. Rev.* **2018**, *47*, 1822–1873.
40. Devasenathipathy, R.; Mani, V.; Chen, S.M.; Viswanath, B.; Vasanth, V.; Govindasamy, M. Electrodeposition of gold nanoparticles on a pectin scaffold and its electrocatalytic application in the selective determination of dopamine. *RSC Adv.* **2014**, *4*, 55900–55907.
41. Chiang, H.C.; Wang, Y.; Zhang, Q.; Levon, K. Optimization of the electrodeposition of gold nanoparticles for the application of highly sensitive, label-free biosensor. *Biosensors* **2019**, *9*, 50.
42. Lin, T.H.; Lin, C.W.; Liu, H.H.; Sheu, J.T.; Hung, W.H. Potential-controlled electrodeposition of gold dendrites in the presence of cysteine. *Chemical communications* **2011**, *47*, 2044–2046.
43. Marcano, D.C.; Kosynkin, D.V.; Berlin, J.M.; Sinitskii, A.; Sun, Z.; Slesarev, A.; Alemany, L.B.; Lu, W.; Tour, J.M. Improved synthesis of graphene oxide. *ACS Nano* **2010**, *4*, 4806–4814.
44. Pei, S.; Cheng, H.M. The reduction of graphene oxide. *Carbon* **2012**, *50*, 3210–3228.
45. Benvidi, A.; Firouzabadi, A.D.; Moshtaghian, S.M.; Mazloum-Ardakani, M.; Tezerjani, M.D. Ultrasensitive DNA sensor based on gold nanoparticles/reduced graphene oxide/glassy carbon electrode. *Anal. Biochem.* **2015**, *484*, 24–30.

46. De la Llave, E.; Clarenc, R.; Schiffrin, D.J.; Williams, F.J. Organization of alkane amines on a gold surface: Structure, surface dipole, and electron transfer. *J. Phys. Chem. C* **2014**, *118*, 468–475.
47. Olmos-Asar, J.A.; Ludueña, M.; Mariscal, M. Monolayer protected gold nanoparticles: The effect of the headgroup—Au interaction. *Phys. Chem. Chem. Phys.* **2014**, *16*, 15979–15987.
48. Hu, Q.; Wang, Q.; Kong, J.; Li, L.; Zhang, X. Electrochemically mediated in situ growth of electroactive polymers for highly sensitive detection of double-stranded DNA without sequence-preference. *Biosens. Bioelectron.* **2018**, *101*, 1–6.
49. Saadati, A.; Hassanpour, S.; de la Guardia, M.; Mosafer, J.; Hashemzaei, M.; Mokhtarzadeh, A.; Baradaran, B. Recent advances on application of peptide nucleic acids as a bioreceptor in biosensors development. *TrAC Trends Anal. Chem.* **2019**, *114*, 56–68.
50. Azimzadeh, M.; Rahaie, M.; Nasirizadeh, N.; Ashtari, K.; Naderi-Manesh, H. An electrochemical nanobiosensor for plasma miRNA-155, based on graphene oxide and gold nanorod, for early detection of breast cancer. *Biosens. Bioelectron.* **2016**, *77*, 99–106.
51. Povedano, E.; Montiel, V.R.V.; Valverde, A.; Navarro-Villoslada, F.; Yáñez-Sedeño, P.; Pedrero, M.; Montero-Calle, A.; Barderas, R.; Peláez-García, A.; Mendiola, M.; et al. Versatile electroanalytical bioplatfroms for simultaneous determination of cancer-related DNA 5-methyl-and 5-hydroxymethyl-cytosines at global and gene-specific levels in human serum and tissues. *ACS Sens.* **2018**, *4*, 227–234.
52. Xiao, L.; Xu, L.; Gao, C.; Zhang, Y.; Yao, Q.; Zhang, G.J. A MoS<sub>2</sub> nanosheet-based fluorescence biosensor for simple and quantitative analysis of DNA methylation. *Sensors* **2016**, *16*, 1561.
53. Khodaei, R.; Ahmady, A.; Khoshfetrat, S.M.; Kashanian, S.; Tavangar, S.M.; Omidfar, K. Voltammetric immunosensor for E-cadherin promoter DNA methylation using a Fe<sub>3</sub>O<sub>4</sub>-citric acid nanocomposite and a screen-printed carbon electrode modified with poly (vinylalcohol) and reduced graphene oxide. *Microchim. Acta* **2019**, *186*, 1–12.